A New Lithium-Rich Zeolitic 10-MR Zincolithosilicate MZS-1 Hydrothermally Synthesized under High Pressure and Characterized by 3D Electron Diffraction

Gwladys Steciuk, Oliver Schäf, Laurence Tortet, Hélène Pizzala, Lukas Palatinus, Wolfgang Hornfeck, Jean-louis Paillaud

A New Lithium-Rich Zeolitic 10-MR Zincolithosilicate MZS-1 Hydrothermally Synthesized under High Pressure and Characterized by 3D Electron Diffraction

Gwladys Steciuk,*[a] Oliver Schäf+,[b] Laurence Tortet,*[b] Hélène Pizzala,[c] Lukáš Palatinus,[a] Wolfgang Hornfeck,[a] and Jean-Louis Paillaud*[d,e]

[a] *Dr. G. Steciuk, Dr. L. Palatinus, Dr. W. Hornfeck, Institute of Physics of the AS CR, v.v.i., Na Slovance 2, 182 21 Prague, Czech Republic E-mail: steciuk@fzu.cz, https://www.fzu.cz*

[b] *Dr. O. Schäf,+ Dr. L. Tortet, Laboratoire MADIREL, UMR7246, Aix-Marseille Université, CNRS, Campus Scientifique de St. Jérôme, 20, 13397 Marseille Cedex France, E-mail: laurence.tortet@univ-amu.fr, https://madirel.univ-amu.fr/*

[c] *Dr. H. Pizzala, Institut de Chimie Radicalaire, UMR7273, Aix-Marseille Université, CNRS, Campus Universitaire de Saint-Jérôme, 52 Avenue Escadrille Normandie Niemen, 13013 Marseille, France, https://icr-amu.cnrs.fr*

[d] *Dr. J.-L. Paillaud, Institut de Science des Matériaux de Mulhouse (IS2M), UMR 7361 CNRS, Université de Haute-Alsace, 68100 Mulhouse, France, E-mail: jean-louis.paillaud@uha.fr, https://www.is2m.uha.fr/en/home-2/*

[e] *Dr. J.-L. Paillaud, Université de Strasbourg, Strasbourg, France*

* Corresponding authors.

+ We dedicate this paper to the memory of our colleague and friend Oliver Schäf, who died on Thursday, March 19th 2020, after the most courageous battle with cancer. Oliver was the promoter of this work and more generally of work on the high-pressure synthesis of zeolites, for which he has given a great deal.

To cite this article: A New Lithium-Rich Zeolitic 10-MR Zincolithosilicate MZS-1 Hydrothermally Synthesized under High Pressure and Characterized by 3D Electron Diffraction, Eur. J. Inorg. Chem. 2021, 628–638. DOI : 10.1002/ejic.202000939, HAL : hal-03142676.
Received 8 October 2020; Received in revised form 11 January 2021; Available online 14 January 2021

Keywords: High pressure hydrothermal synthesis · Lithium ·Superstructures · Zeolites · Zinc

ABSTRACT: We report the structure of a new high lithium content zincolithosilicate (MZS-1) obtained after hydrothermal treatment under high pressure from a glass precursor. After synthesis microcrystalline mixture of phases was obtained among which the main phase was unknown. Due to the sub micrometric size of the crystallites its structure was determined from precession-assisted 3D electron diffraction measured at 100 K and refined using the dynamical theory of diffraction. More accurate lattice parameters are obtained from Rietveld refinement of synchrotron powder data collected at the ambient temperature. The characteristic framework is described at the ambient temperature using an average unit cell a_0 = 8.57999(5) Å, b_0 = 14.12332(8) Å, c_0 = 4.96827(3) Å in the space group *Ccc*2. The structure of the new zeolitic 10-membered ring zincosilicate with chemical formula per unit cell $(SiO_2)_2Zn_{0.408}LiO(OH)_2(Li,H)_{2.184}$ (Z = 4) is composed of undulated silicate layers made of fused 6-membered rings connected via vertices of $(Zn,Li)O_4$ tetrahedra. A weak superstructure doubling the a0 parameter is observed and is explained by a Zn/Li ordering within the $(Zn,Li)O_4$ layers.

Introduction

Zeolites are crystalline silicate-based materials built by cornersharing TO_4 tetrahedra (T = Si, Al, P, etc.).[1] Among them, microporous zincosilicates containing zinc as a structural element of the framework are potentially interesting due to their catalytic behavior[2] and for biochemical applications.[3] In silicate-based materials, the incorporation of $[ZnO_4]^{2-}$ into the silica framework instead of $[AlO_4]^{1-}$ or SiO_4 creates two anionic sites per zinc atom that is a way to tune properties of cation exchanger materials or acidic properties.[4] Moreover, ZnO_4 tetrahedra present a higher flexibility: larger T–O bond-length and O–T–O angle distortions. It allows the formation of lower framework densities material containing, e. g., 3-membered rings (3-MRs) and spiro-groups.[5] In nature, the mineral gaultite[6] $Na_4Zn_2Si_7O_{18}·H_2O$ (Si/Zn = 3.5) is the only silicate-based zeolite known with Zn^{2+} as framework T-atom. Previous works show that the synthesis of gaultite is possible under highpressure hydrothermal conditions[7] and several other synthetic zeolitic zincosilicates prepared under conventional hydrothermal conditions also exist.[8] However, the incorporation of Zn into the framework of highly siliceous zeolites without the concomitant incorporation of Al is a challenge. VPI-7 was the first one reported by Annen et al. (1991).[9] It has topology VSV[10] and is in fact the synthetic counter-part of gaultite. Later, more members of this zeolitic zincosilicates family where prepared including, among many others, RUB-17 (RSN-type),[5b] VPI-9 or VPI-10.[5a] Because lithium has an ionic radius almost identical to zinc and beryllium, Park et al. explored the possibility to introduce Li^+ as framework cation by using a reaction mixture close to the one of RUB-17, with Cs^+ and Li^+ as Group I cation.[11] They obtained RUB-23, a microporous lithosilicate that forms a 3D silicate framework containing Li^+ cations in T sites at the centre of spiro-5 units (Figure 1). The negative net charge of the framework is here counterbalanced by extra-framework caesium, lithium and hydrogen cations. Such Li, Si-spiro-5 units are also found in RUB-29, a microporous lithosilicate with a high ratio of Li to Si (1 : 4)[12] and more recently, in AES-7, a lithium-containing calcosilicate with ratio Li/Si ≈ 1/8 synthesized via the hydrothermal treatment of a mechanochemically

prepared precursor under autogenous pressure.[13] All these studies show the challenge in synthetizing new zincosilicate zeolitic material with high Li content as part of the framework.

In hydrothermal synthesis, it is not exceptional to obtain multiphasic powders with average crystal size below one micron. In such case, neither the powder x-ray diffraction (PXRD) nor other conventional characterization technique will allow a detailed structure analysis or appropriate phase identification. Fortunately, the advances achieved over the last decade in technology as well as in theoretical aspects of structure analysis by 3D electron diffraction (3D ED)[14,15] open the door for complete structural characterization of submicron sized crystals, even for complex and disordered structures such as those found in the domain of zeolites. Indeed, since the advent of 3D ED methods,[14b–d,15] conveniently combined with precession electron diffraction (PED),[16] several zeolite structures such as IM-17[17] (**UOV**-type) and IM-18[18] (***UOE**-type) have been solved. Moreover, for sufficiently well crystallized materials, an accurate structure refinement from precession electron diffraction tomography (PEDT) data is now possible when the dynamical-diffraction effects are properly considered.[19] The possibility to use the 3D ED data collected at the nanoscale for the refinement is a key when the PXRD data is not suitable (overlaps, weak superstructures, secondary phases, etc.).[20] For phases with lower crystallinity, the structural model obtained from 3D ED experiments can be combined with complementary technics. Multiple examples can be cited. For IM-18, the average structure was determined from rotation electron diffraction (RED)[14d] data and high resolution transmission electron microscopy (HRTEM) was employed to characterize the stacking disorder.[18a] The presence of defects in the polycrystalline sample of IM-18 was proved and quantitatively explored by combining ^{29}Si magic angle spinning (MAS) NMR and ^{1}H–^{1}H double quantum MAS NMR spectra with computational simulation.[18b] More recently, the structure of THK-2 was solved from 3D ED and combined with PXRD.[5c] In this work, starting from a glass precursor containing lithium, zinc and silicon species and a high pressure hydrothermal procedure,[7a] we obtained a multiphasic microcrystalline mixture in which the main phase is a new zincolithosilicate (volume fraction ≈ 90%). Using the advantages of hydrothermal synthesis and the high flexibility of ZnO_4 tetrahedra, a very high amount of Li was introduced in the framework substituting Zn sites. The structure of the new phase MZS-1 was solved and refined from 3D ED data collected in precession mode using the dynamical refinement method. The refinement from 3D ED data reveal fine details of the structure possessing Li as part of the framework, OH/H_2O groups in the pore as well a weak ordering that could not be identified from synchrotron powder diffraction data. The refinement combined with Thermogravimetric analysis and solid-state NMR confirm the existence of Li intra framework and brings to light the potential properties of this material through the characterization of the pore content.

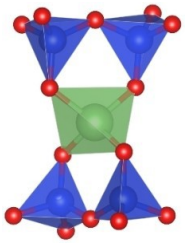

Figure 1. The spiro-5 unit of composition $[Si_4LiO_{14}]^{11-}$ present in RUB-23. Lithium (green) is here at the spiro-position.[11]

Preliminary characterizations

A global view of the as-synthesized sample prepared at 145°C (Figure 2A) shows the multiphasic nature of the product with distinct morphologies. The majority of particles are elongated crystals with inhomogeneous thicknesses even on the same crystal that suggests a lamellar structure (Figure 2B). These crystals are responsible for the main diffraction peaks on the PXRD pattern (see below). The EDX elemental analysis performed in the TEM (Figure S1) shows that the phase of interest has a Si/Zn ratio ranging from 3.84 to 8.55 with a median value of 4.86. The average value obtained from the 9 measurements is 5.57. The crystals with Si/Zn of about 1.18 presenting elongated lens shape in Figure S1 correspond to the secondary phase $Zn_{1.1}Li_{0.6}Si_{1.3}O_4$.

Two main pieces of information emerge from the PXRD diagrams (Figure 3). First, for both temperatures of synthesis (80 and 145°C) the PXRD patterns are similar except for the absence of quartz in the sample synthesized at 80°C. Secondly, in the 80°C sample, the X-ray reflections are broader, indicating a smaller crystallite size in comparison with the product prepared at 145°C. Due to the better crystallinity, the product prepared at 145°C was preferred for the structural study despite the presence of quartz and the product prepared at 80°C was used for solid-state NMR analysis. The high-temperature PXRD (Figure S2) of the product synthesized at 80°C (with no quartz) shows a net decrease in peak intensity above 200 °C and a complete destruction of the structure followed by its transformation into amorphous materials and not well crystallized LiZn- and Li-silicates. This behavior under such heat treatment is similar to that observed in the case of AES-7.[13]

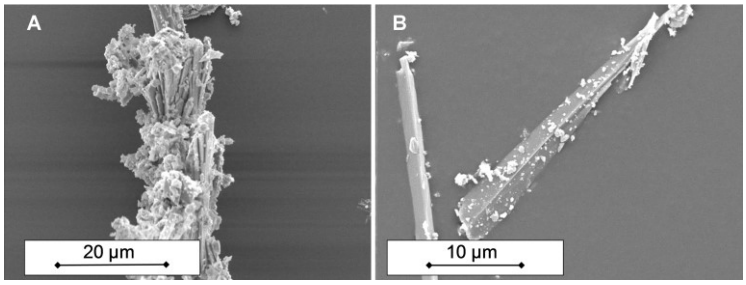

Figure 2. SEM micrographs of the synthesized product at 145°C containing the new zincosilicate, (a) global view, (b) magnified view showing the main phase.

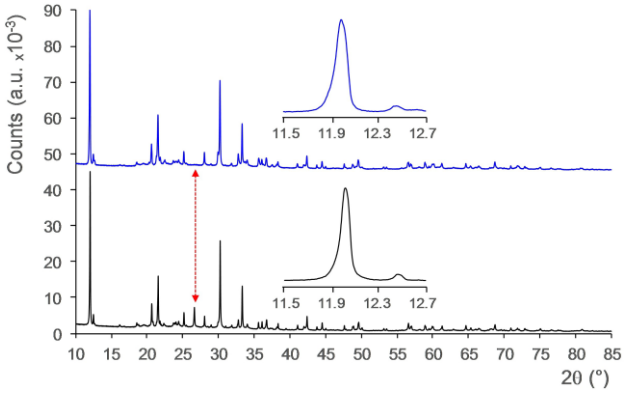

Figure 3. Laboratory PXRD diagrams of the products obtained at 80°C (blue) and at 145°C (black). The dotted red arrow points to the position of the most intense (101) reflection of quartz in the sample synthesized at 145°C and its quasi total absence in the sample prepared at 80°C. The inserts highlight a broader FWHM for the main reflection of the new phase when prepared at 80°C.

Because of the multiphasic nature of the product, full indexing of the laboratory PXRD pattern (Figure 3) was not achieved even after elimination of the well recognizable reflections of quartz. However, the most intense reflections yielded an orthorhombic unit cell with a_0 = 8.553(8) Å, b_0 = 14.1432(10) Å, c_0 = 4.9721(4) Å and V_0 = 604.03(11) Å^3, which allowed a satisfactory fit of the powder pattern. The observed systematic extinctions on the selected reflections indicated a C centered lattice. Unfortunately, neither direct methods nor the charge-flipping algorithm provided a solution of the crystal structure from the powder pattern despite the relatively small volume of the unit cell. This failure is due to overlaps of the reflections coming from the main phase with those of the secondary phases. Therefore, we have decided to study the new phase by single crystal 3D ED (Figure 4).[20]

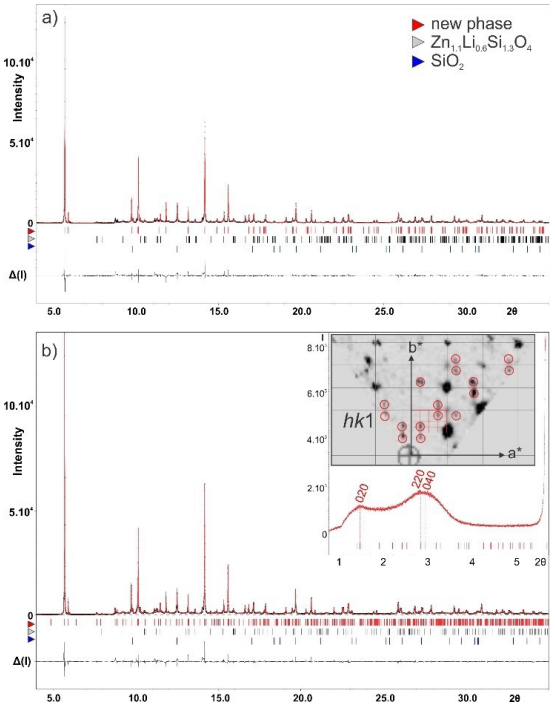

Figure 4. Rietveld refinement against synchrotron data of (a) the average structure (*Ccc*2) and (b) the superstructure (*Pcn*2). In the insert is the low angle region of the diagram and the section hk1 from 3D ED showing the existence of another weak and poorly crystallized superstructure.

The broad resonance observed on the ^{7}Li MAS NMR spectrum near 0 ppm presents an asymmetry (Figure 5). This signal can be deconvoluted into two components of distinct widths at 0.28 and -0.24 ppm suggesting at least two distinct tetrahedral sites. Their proportion, by taking into account the spinning side bands, are 60% and 40%, respectively. Similar spectra were observed for RUB-23,[11] RUB-29,[12] the lithosilicate RUB-30[21] and more recently for AES-7[13] and THK-2.[5c] In all these cases, the lithium cations are located in the center of LiO_4 tetrahedra with probably two slightly different environments.

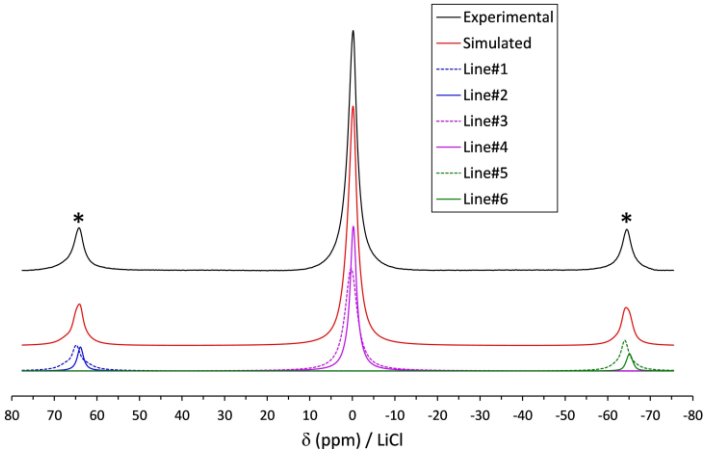

Figure 5. ^{7}Li MAS NMR spectrum of the sample synthesised at 80°C showing the asymmetry of the resonance. The spinning side bands marked with a * have been included in the decomposition.

Structure determination from 3D electron diffraction

The 3D ED data were collected and analyzed on all phases found during the experiment. Most of crystals belong to the new phase with blade-shaped crystals (Figure 2B and Figure S3). The 3D ED experiments also show the presence of alpha-quartz SiO_2 ($P3_221$)[22] and $Zn_{1.1}Li_{0.6}Si_{1.3}O_4$ ($P2_1/n$),[23] later confirmed on PXRD data. No further details about the 3D ED analysis of these phases are given in this work as they are known. Another unknown poorly crystalline phase containing Li, Zn and Si was measured that may correspond to the disordered features visible in the synchrotron powder diffraction diagram at low angles (Figure 4). Unfortunately, this last phase(s) was(were) not sufficiently crystalline to allow a complete characterization by the 3D ED methods.

Based on 3D ED data measured at 100 K, the new zeolite has an average orthorhombic lattice $a_0 \approx 8.55$ Å, $b_0 \approx 14.01$ Å and $c_0 \approx 4.94$ Å, values close to those determined from PXRD at the ambient temperature (Figure 6a). The space group was determined from the sections of the reciprocal space (Figure 6b) combined with the synchrotron powder diagram (Figure 4a).[24] The condition hkl: $h+k = 2n$ confirms the expected *C*-centering of the lattice. Two *c*-glide planes are present perpendicular to a and b-axis respectively (0*kl*: $l = 2n$ and *h*0*l*: $l = 2n$). The weak reflections with $l = 2n+1$ visible in the sections 0*kl* and *h*0*l* are explained by residual dynamical effects and the presence of a weak superstructure doubling the vector a of the average lattice (see below). The observed reflection conditions suggest the space groups *Cccm* or *Ccc*2. Structure solution by the program Superflip,[25] and subsequent symmetry analysis of the solution, which is independent of the space group estimation from the diffraction pattern, revealed that the structure has a non-centrosymmetric space group *Ccc*2.

In Figure 6a and Figure 6b, weak reflections are found that correspond to the doubling of the parameter a_0. The superstructure is described in the supercell $2a_0 \times b_0 \times c_0$. The superstructure reflections are not well visible in all the measured crystals and they are associated with diffuse features along **b*** in most of data. Because of the presence of dynamical diffraction in the ED data together with non-identified peaks in the synchrotron powder diffraction data, the determination of symmetry solely from experimental data was challenging. Therefore, the evaluation of the supercell symmetry relies on the group-subgroup relationships with the space group of the average structure combined with the available data (Figure 6b). Nevertheless, ED data show clearly that the doubling of the unit-cell along the a-axis breaks the *C*-centering while the cglide plane perpendicular to the a-axis is maintained. The subgroup of *Ccc*2 with the highest symmetry and consistent with these observations is *Pcn*2. The synchrotron powder data is consistent with the *n*-glide perpendicular to *b* despite that the ED data exhibits some weak violations of the systematic absences due to the *n*-glide. Consequently, the structure is described in the space group *Pcn*2. Note that from the 3D ED data collected at 100 K, another superstructure variant was observed in one crystal (insert in Figure 4). Though as observed in Figure 4, the additional superstructure reflections were too weak and diffuse to be quantitatively analyzed. This minor ordering gives a unit cell equal to $4a_0 \times 4b_0 \times 2c_0$ that corresponds to the very broad peaks at low angles on the powder data.

The average structure was solved from 3D ED data collected at 100 K which yielded data with 99.73% completeness up to the resolution of 0.7 Å. The most important experimental parameters are listed in Table 1. The structure solution was performed ab initio using the charge flipping algorithm[25a,26] implemented in the program Superflip.[25b] The solution provided by Superflip is a 3-dimensional map of the electrostatic potential (e-map, Figure 7a). The e-map shows a tetrahedral framework of general composition TO_2 (T = Si, Zn) with the presence of two main cationic sites S1 and S2. The distances S1-oxygen between 1.57 Å and 1.65 Å indicate that S1 is occupied by Si. The longer distances S2-oxygen 1.86–2.03 Å are characteristic for Zn–O or Li–O. The electrostatic potential of S2 is weaker than S1 indicating a partial occupancy of S2 by Zn or a mixed Li/Zn occupancy. Another cationic site S3 is revealed from the difference potential map after the first kinematical refinement (Figure 7b). With a distance S3–O between 1.85–2.02 Å, this atomic site can also be attributed to Zn or Li with a partial occupancy. Yet another tetrahedral site can be identified in the structure (labelled S4 in Figure 7b). The distances to the oxygen positions (around 2 Å) are also compatible with Zn or Li atom. This site, however, shows no significant potential maximum in the kinematical difference map.

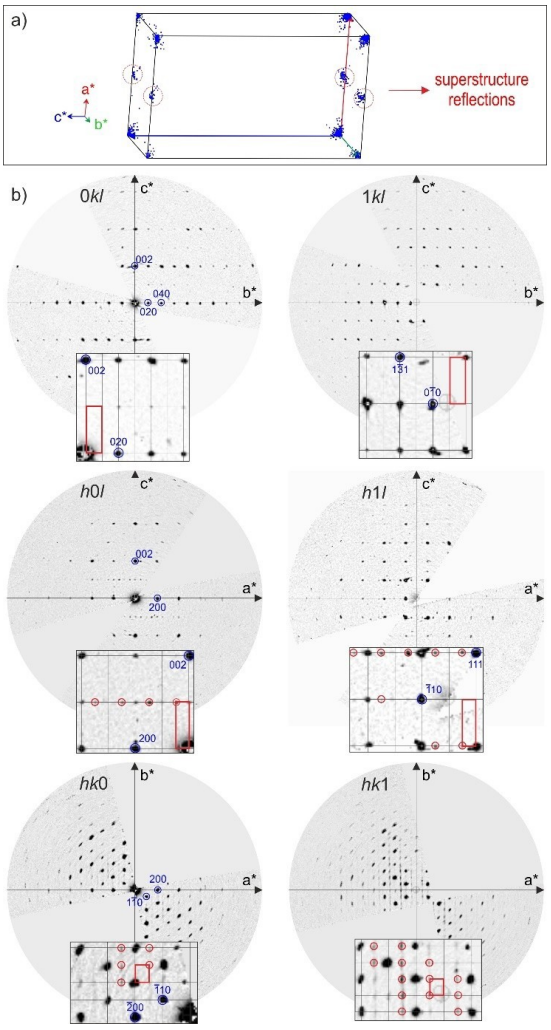

Figure 6. (a) Reciprocal space projected in one average unit cell. The superstructure reflections corresponding to $a = 2a_0$ are encircled in red. (b) Sections of the reciprocal space. Black grid shows the reciprocal lattice corresponding to the average unit cell. The reflections and the unit cell corresponding to the superstructure are represented in red.

The average structure was refined from the 3D ED single crystal data using the dynamical refinement method, which takes the dynamical diffraction effects into account without restriction on cation-oxygen distances.[19] Several tests were carried out to determine the presence and the amount of Zn and/or Li in the two partially occupied S2 and S3 sites. In this case, it was not possible to freely refine the occupancies of mixed sites in S2 and S3 because none of them is fully occupied. Furthermore, restrictions on Li/Zn ratio are difficult to set with confidence as the total amount of Li is unknown. Tests with different Li/Zn ratios in S2 and S3 were done. They show that S2 = Zn is a very good approximation as the introduction of a small amount of Li in S2 results in unrealistic displacement parameters and a significant increase of the *R*-factors. More ambiguous results are obtained for S3: the refinements with S3 = Li and S3 = Zn produce similar *R*-factors with occupancies of about 0.5 and 0.165 respectively. However, the isotropic atomic displacement parameters (isotropic ADPs) when S3 = Zn is very high (Uiso(S3 = Zn) = 0.092 $Å^2$) while they remains at reasonable values for S3 = Li (Uiso(S3 = Li) = 0.013 $Å^2$). Furthermore, with S3 = Zn (≈ 16.5% occupied), the ratio Si/Zn ≈ 2.61 is not within the range determined by EDX (from 3.84 to 8.55) and what is observed by ^{7}Li MAS NMR is difficult to explain. Consequently, although it is not possible to exclude a small amount of Li in S2 and Zn in S3, the refinement tests show that the best approximation is S2 = Zn and S3 = Li.

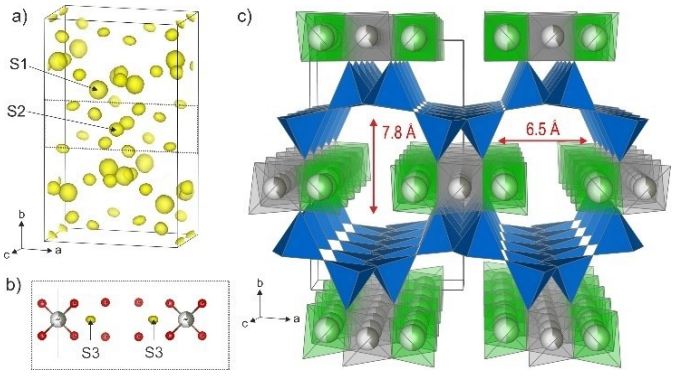

Figure 7. (a) Projection of the 3D electrostatic potential map with the two main cationic sites S1 and S2. (b) In the encircled area S3 revealed (3σ isosurface) from the kinematical refinement. (c) Perspective view of average structure framework refined dynamically against 3D ED data considering S4 as empty.

Table 1. Summary of 3D PED data collection conditions and refinement parameters for the average structure and the superstructure.

Settings	Average structure	Superstructure
Refined formula		$(SiO_2)_2Zn_{0.408}LiO(OH)_2(Li,H)_{2.184}$
a_0	8.55 Å	$2a_0$
b_0	14.01 Å	b_0
c_0	4.94 Å	c_0
V_0	591.74 Å^3	$2V_0$
Z	4	*8*
Space group	*Ccc*2 (#37)	*Pcn*2 (#30)
Data collection		TEM Philips CM120
Source wavelength		0.0335 Å
Collection mode		Precession-assisted 3D ED
T of measurement		100 K
Limiting θ angles		0.64°–1.34°
Limiting Miller indices	$0 \le h \le 11$; $0 \le k \le 19$; $-6 \le l \le 6$	$0 \le h \le 23$; $0 \le k \le 19$; $-6 \le l \le 6$
N(obs/all)indep.(kin)	657/857	979/3373
Data completeness for $sin\theta/\lambda$ = 0.7 Å^{-1}	99.73%	99.36 %
R_{int}(obs/all)(kin)	14.05%/14.72%	15.90 %/22.70 %
Redundancy	2.212	2.259
Kinematical refinement		
N(obs/all)	674/841	984/3373 *h* = 2*n*: 709/1682 *h* = 2*n* + *1*: 275/1691
R(obs)/*wR*(obs)	15.97 %/19.95%	all: 17.59 %/19.90% *h* = 2*n*: 15.92 %/19.38 % *h* = 2*n* + *1*: 29.33 %/24.67 %
N param.	25	42
Dynamical integration and refinement		
N(obs/all)	1757/3255	2420/13818 *h* = 2*n*: 1923/6814 *h* = 2*n* + *1*: 497/7004
RSg(max)	0.6	0.6
R(obs)/*wR*(obs)	7.76 %/7.95%	All: 10.88 %/11.20% *h* = 2*n*: 8.92 %/9.43% *h* = 2*n* + *1*: 25.26 %/27.70%
N param. (structure)	58	67
N param. (all)	157	162
Crystal thickness	400(3) Å	407(2)

The occupancies of Zn and Li were then freely refined. It first leads to occupancies of 0.405(5) and 0.536(12) for Zn and Li respectively. The occupancy of S3 was later set to 0.5 because the distance between neighboring cations Zn and/or Li hinders an occupancy above 0.5 for S2 and S3. After the first refinement step, one hydrogen position was revealed from the difference potential map (Figure 8a).[27] While the apparent O–H distance is still an open question in electron diffraction,[28] this distance was restricted around 1 Å and the ADPs

for hydrogen was set as riding with an extension factor of 1.2. The final refinement with hydrogen gives *R(obs)/wR(obs)* = 7.76%/7.95% for 1757/3255 observed/all reflections and 157 refined parameters. The refinement parameters are presented in Table 1 and the structural parameters in Table S1. The resulting structural model is presented in Figure 7 and the topology of the individual layers in Figure 9. The refined amount of Zn corresponds to the ratio Si/Zn = 4.91(1), in agreement with the chemical analysis by EDX, which indicates a median ratio of 4.86. For Z = 4, the amount of Zn in S2 is about 0.408(5) and the number of Li in S3 is close to 1, yielding the composition $(SiO_2)_2Zn_{0.48}LiO(OH)_2$ (Table 1). This formula is not charge balanced with a missing charge of +2.184. The missing charge can be explained either by an additional proton on the OH group, making it a water molecule, or the presence of Li in the last tetrahedral sites S4 formed by O4. However, the difference potential map obtained from 3D ED refinement showed a very weak residual potential in the S4 site elongated along *c*. This indicates that only a small amount of Li is detected in S4 and most of the OH groups are in fact H_2O. The amount of Li in S4 could not be successfully refined using the dynamical approach as it is disordered.

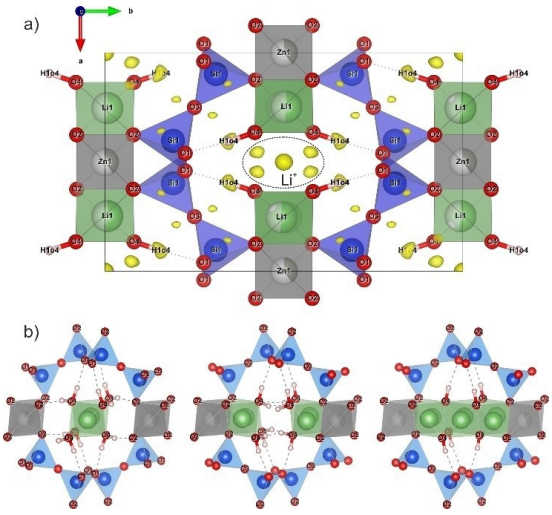

Figure 8. (a) Projection of the average structure along the c-axis with a superimposed difference potential map showing maxima at the position of the hydrogen atom. Isosurface levels are 2σ[ΔV(r)] (yellow). (b) Possible configurations to ensure a bond valence sum ≈ 2 vu for O4.

A Rietveld refinement of the average structure was performed using synchrotron powder data in JANA2006 including the secondary phases SiO_2 (5.2%) and $Zn_{1.1}Li_{0.6}Si_{1.3}O_4$ (4.8 %). This refinement confirms that the model obtained from single crystal ED data is representative at the powder scale since all the most intense reflections are indexed using the average unit cell (Figure 4a). The main phase represents around 90% of the sample. The refinement gives *R(obs)* = 0.0489, *wR(obs)* = 0.0651, *GOF* = 0.0428, *Rp* = 0.0878 and *wRp* = 0.1301 with 486 observed reflections and 21 refined structural parameters (Table S2 and Table S3). Unlike the dynamical refinement of 3D ED data, restrictions were applied on cation- oxygen distances and the hydrogen position could not be determined from the difference Fourier map.

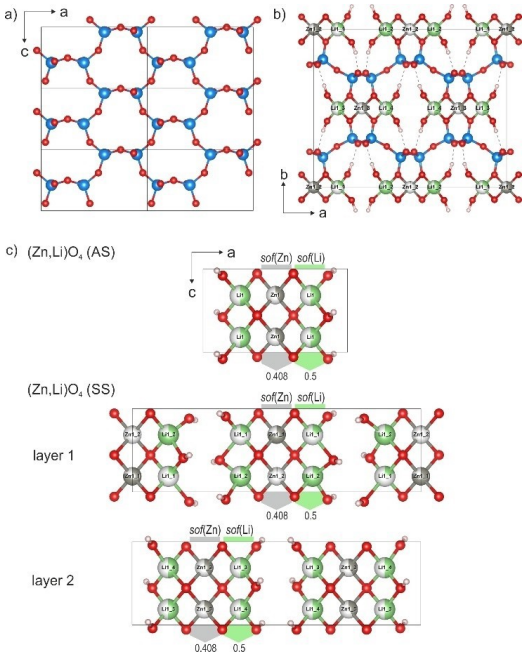

Figure 9. (a) View down [010] and [001] of the SiO_4 layer in the average and the supercell description. (b) Representation of the super structure after the dynamical refinement from 3D PED data. (c) [010] projections of the $(Zn,Li)O_4$ layers in the average model and in the superstructure. The *s.o.f.* (Zn) and *s.o.f.* (Li) are the average occupancies in each column along *c*.

In order to understand the origin of the ordering responsible for the superstructure reflections along a, the superstructure was solved in the supercell $2a_0 \times b_0 \times c_0$ (*Pcn*2) from a crystal where enough superstructure reflections *h* = 2n + 1 were significant ($I \geq 3\sigma(I)$). The results for the superstructure (SS) are presented as projections of the 3D electrostatic potential in Figure S4. On the [001] and [010] projections of the potential map, the different repartition in the S2 (Zn1-1, Zn1-2, Zn1-3) and S3 (Li2-1, Li2-2, Li2-3 and Li2-4) sites creates two different $(Zn,Li)O_4$ layers instead of the single $(Zn,Li)O_4$ layer in the average structure. The phenomenon is more obvious for S2 sites occupied by Zn. The change also affects position of the O4 (OH or H_2O) atom along c that belongs to the $(Zn,Li)O_4$ layer. In contrast, the SiO_4 layers do not show significant change.

As for the average model, the superstructure was refined against 3D ED data. The superstructure reflections *h*=2n+1 are only observed at low resolution with weak intensities and tend to be elongated along *b* (out of the Bragg position). The dynamical refinement as well as the kinematical one cannot consider the diffuse scattering, and in general, all the inelastic scattering events.[29] For the reasons mentioned above, the refinement of the superstructure has to be interpreted carefully as its accuracy is lowered. It is now well known that dynamical

refinement reaches its best accuracy for well crystallized samples. The presence of diffuse features causes less pronounced dynamical effects and the results of the kinematical refinement is also considered.

The initial superstructure model was first solved from the charge flipping algorithm (SUPERFLIP). However, for the refinements the starting superstructure model is obtained from the refined average structure by doubling the a_0 parameter and then lowering the symmetry to *Pcn*2. Moreover, in order to stabilize the refinements and focus on the superstructure, only the parameters affected by the superstructure are refined. The initial superstructure model suggests that these two environments are created by the Zn/Li ordering and not by the rotation of the SiO_4 tetrahedra (S1, O1, O2, O3). Therefore, the atomic positions related to the four SiO_4 tetrahedra in the superstructure are constrain to keep the symmetry of the average structure. Same strategy was applied to the atomic positions S2 (from Zn1-1 to Zn1-3) and S3 (from Li1-1 to Li1-4) in the superstructure. The O4 positions (O4-1 to O4-4) are freely refined as a variation of the position is observed especially along the c-axis on the electrostatic potential map of the supercell. The refinement of the ADPs was performed as well as the occupancies of the Zn and Li sites. The refined amount of Zn and Li of the average structure is maintained by setting the overall occupancies of S2 = 0.408 (Zn1-1, Zn1-2, Zn1-3) and S3 = 0.5 (Li1-1, Li1-2, Li1-3, Li1-4) as well as in each layer by setting *s.o.f.*(Zn1-1) + *s.o.f.*(Zn1-2) = 0.480, *s.o.f.*(Li1-1) + s.o.f.(Li1-2) = *s.o.f.*(Li1-3) + *s.o.f.*(Li1-4) = 1 and *s.o.f.*(Zn1-3) = 0.480 (see Figure 9c). To prevent two neighbouring Li and Zn cations from being present at the same time, we assume *s.o.f.*(Li1-1) = 1 - *s.o.f.*(Zn1-1). The last restriction was set because, when freely refined (kinematical or dynamical), s.o.f.(Li1-1) takes values slightly above 1 - *s.o.f.*(Zn1-1). No restriction was necessary between Zn1-3 and the neighbouring Li1-3 and Li1-4. After the first refinement steps without hydrogen, the 4 hydrogen positions were revealed close to O4 from the difference potential map at same positions than for the average structure (from O4-1 to O4-4) showing that this hydrogen position is not affected by the supercell.

The dynamical refinement leads to *R(obs)/wR(obs)* = 0.1088/0.112 for 2420/13818 observed over all reflections with *R(obs)/wR(obs)* = 0.2526/0.2770 for the 275 reflections h = 2n + 1 and 67 refined structural parameters. The results of the dynamical refinements are presented in Table 1. The representation of the refined superstructure is shown in Figure 9b and the corresponding structural parameters are presented in Table S4. The huge difference in the *R*-factors observed for the superstructure reflections *h = 2n + 1* is explained by their very weak intensities and their rather diffuse nature as mentioned before. This issue in the refinement was already observed in vaterite $CaCO_3$ that also presented weak and diffuse superstructure reflections.[30] Regarding the occupancies, the dynamical and the kinematical refinements give similar results (Table 2). The S2 site with s.o.f.(Zn1) = 0.408(5) in the average structure is spread between three cationic sites in the superstructure with *s.o.f.*(Zn1-1) = 0.788(2), *s.o.f.*(Zn1-2) = 0.028(2) and *s.o.f.*(Zn1-3) = 0.408. In the same way S3 is distributed into 4 sites with *s.o.f.*(Li1-1) = 0.212(2), *s.o.f.*(Li1-2) = 0.788(2), *s.o.f.*(Li1-3) ≈ *s.o.f.*(Li1-4) ≈ 0.5 (Table 2 and Figure 9c). The configurations of the two (Zn, Li)O_4 layers in the superstructure is shown in Figure 9c.

Table 2. Summary of the site occupancies from the different refinements in the average (AC) and the supercell (SC).

AC			SC		
Site	SP	*Dyn./Kin.*	*Site*	*Kin.*	*Dyn.*
Zn1	0.4823(8)	0.408(5)	Zn1-1	0.804(6)	0.788(2)
			Zn1-2	0.012(6)	0.028(2)
			Zn1-3	0.408	0.408
Li1	0.595(3) then set to 0.5	0.536(12) then set to 0.5	Li1-1	0.196(6)	0.212(2)
			Li1-2	0.804(6)	0.788(2)
			Li1-3	0.509(15)	0.507(5)
			Li1-4	0.491(15)	0.493(5)

Despite the very satisfactory results obtained for the average model, the refinement from synchrotron powder data of the superstructure does not give relevant results. Although the refinement leads to reasonable *R*-factors (see Table S2), the superstructure reflections are too weak and overlap with several weak unindexed peaks. Moreover, remaining weak unindexed reflections strongly suggest the presence of even more secondary phases at the ambient temperature likely including other ordering variants as it was observed in some 3D ED data (Figure 4).

The ^{29}Si MAS NMR spectrum of the multiphasic sample prepared at 80°C (see Figure S5) shows two main resonances at chemical shifts at -91.3 and -91.8 ppm that could correspond to two types of Q_4 silicon of type $Si(OSi)_3(OZn)$ as observed for the tectozincosilicates

VPI-7,[31] VPI-9,[32] and RUB-17.[5b] A broad resonance at -95.2 ppm is also present. Its assignment is, in this case, complicated by the presence of the secondary phases and possibly of a small amount of amorphous or poorly crystalline silica-based species, but it might correspond to different Q_3 species such as $Si(OSi)_3OH$ and/or $Si(OSi)_3O^-$. In the ordered lithium-containing calcosilicate AES-7, for these Q_3 species, a single sharp resonance is observed at -94.7 ppm in the $^1H \rightarrow ^{29}Si$ CP/MAS and ^{29}Si DDMAS NMR spectra.[13] Nevertheless, the presence of several components with variable intensities is due to the disorder of crystallographic sites that change the local chemical environment around the silicon atoms. It is worthy to note that the spectrum does not show a signal for a framework silicon atom shifted to low field as observed for VPI-7, VPI-9 and RUB-17, which is attributed to a Si atom at the centre of a spiro-5 unit. The absence of quartz is also confirmed since its characteristic resonance at -107.4 ppm[33] is not detected. On the CPMAS spectra, a lower intensity gain is observed for the resonances at -91.3 and -91.8 ppm in comparison with the component at -95.2 ppm, the resonance at -91.3 ppm being more affected than the one at -91.8 ppm. These enhancements are attributed to the proximity of the hydroxyl protons of the silanol groups.

Discussion

From 3D ED single crystal analysis, the new zincolithosilicate phase is described in an average orthorhombic Ccc2 space group with lattice parameters a_0 = 8.57999(5) Å, b_0 = 14.12332(8) Å, c_0 = 4.96827(3) Å at room temperature. The dynamical refinement gives very good results (*R(obs)/wR(obs)* = 7.76 %/7.95%) and validates the average model (Table 1). The biggest challenge in this study was to determine the nature of the atoms in the partially occupied S2 and S3 sites and thus, to prove and quantify the presence of Li as a part of the framework. The refinements from all diffraction data (3D ED and synchrotron powder) show better results for S3=Li (half occupied), notably in terms of atomic displacement parameters. However, we cannot exclude the possible presence of a small amount of Li (Zn) in S2 (S3). The presence of Li as part of the framework is also strongly supported by the ^7Li MAS NMR spectrum (Figure 5) that indicates a tetrahedral environment for the lithium cations.[11,13] This singlet is also due to the secondary phases $Zn_{1.1}Li_{0.6}Si_{1.3}O_4$ where Li is in tetrahedral coordination as well as the unknown variant observed in the powder data but in small proportion since the Rietveld refinement converged with a volume fraction of 90% for the main phase. Thereby, it is not unreasonable to think that part of the lithium belongs to the main phase as it was demonstrated experimentally from Xrays and solid-state NMR in the case of the related AES-7 structure. The refined chemical composition of the zincosilicate per unit cell is $(SiO_2)_2Zn_{0.408}Li_1O(OH)_2$, but in order to compensate the net negative charge of the inorganic framework, protons or lithium cations must be introduced in the chemical formula. Thus, the chemical formula becomes $(SiO_2)_2Zn_{0.408}LiO(OH)_2(Li,H)_{2.184}$ (Z = 4). The Si/Zn = 4.9 ratio is in line with the semi-quantitative chemical analysis by EDX on TEM performed on several elongated micro crystals which shows an inhomogeneous chemical composition Si/Zn from 3.84 to 8.55 through the crystals of the same morphology (Figure S1). Moreover, the ratio Si/Li = 2 shows that a very high amount of Li can be introduced in the framework by substitution of ZnO_4 sites. The higher Si/Zn ratio (from 6.93 to 8.55) seems to correspond to more disordered crystals of the main phase.

In term of framework, the new zincolithosilicate is composed of undulated phyllosilicate layers made of fused 6-membered rings in “chair conformation” lying in the (*a,c*)-plane (Figure 7c). The silicate layers are connected to the disordered $(Zn,Li)O_4$ polyhedra via their vertices to form a 1-dimensional straight channel down the c-axis. In the interlayer, ZnO_4 and LiO_4 form adjacent and infinite chains of tetrahedra along c with their occupancies close to half (0.408(5) for Zn1 and 0.5 for Li1). ZnO_4 and LiO_4 are connected with each other along *a*-axis with sharing their edges. The channel is 7.8 Å high and its width depends on the occupancies of the S3 and S4 sites (Figure 7c). Our structure presents strong similarities with AES-7 where even more distorted phyllosilicate layers are connected by Li and Ca in the interlayer.[13] Moreover, in AES-7, Li is also found as part of the framework as well as a compensation cation on the channel. In our structure, the LiO_4 tetrahedra is not present in a spiro-unit like in e. g. RUB-23[11] since they point towards the channel and are connected to the framework (ZnO_4) and to two hydroxyl groups (likely water molecules) present in the channels to complete the coordination sphere. The hydrogen position of the hydroxyl groups (O4) is easily localized in the channel after the refinement in the average structure and in the supercell (Figure 8a). The bond valence analysis indicates that this OH group needs to be stabilized either by lithium in tetrahedral coordination (S3 and S4 sites) and more likely another proton (water molecule) (Figure 8b). Due to the weak scattering power of H and Li, the remaining positions that are partially occupied and likely disordered by the compensation cations in the channel (Li and H) cannot be determined from the refinement. In Figure 8b, three configurations are presented that allow the bond valence sum of O4 to reach 2 vu (valence unit). The two first one show water molecules (O4) in the channel. When Li1 (Li2) is absent, the second hydrogen can point towards O2 (O4) to form water molecule with the angle H1O4-O4-H2O4 ≈ 109 degrees. In the last configuration, the hydroxyl group can be stabilized only when Li1 (S3) and Li2 (S4) are both present to ensure the bond valence sum (BVS) of O4 ≈ 2 vu (if we assume no extra framework Li). The 3D ED data tend to show the likely presence of the two first configurations with water molecules instead of hydroxyl because of the weak amount of Li detected in S4. Moreover, the TGA analysis support this hypothesis since the 11.5% weight loss

observed on the TGA curve (Figure S6) corresponds to the evacuation of approximately 1.6 molecules of zeolitic water. It means that about 75% of the 2.184 positive charges necessary to compensate the net negative framework charge are protons of water molecules. This theoretical water content is also supported by the ^{7}Li MAS NMR spectrum (Figure 5). Considering 25% of the necessary 2.184 positive compensation charges as being Li^{+} located in the center of the channel (site S4 on Figure 7b), the ratio $Li_{("framework")}/Li_{(S4)}$ is then 1/0.546 or 65%/35%, ratio consistent with that of 60%/40% determined by the decomposition of the ^{7}Li MAS NMR spectrum. The difference of chemical environment between both kinds of LiO_4 tetrahedra explained the chemical shift split of ≈ 0.5 ppm, unlike $Li_{("framework")}$, $Li_{(S4)}$ do not share vertices with the SiO_4 tetrahedra as illustrated on Figure 8b.

Although the average structure gives a rather complete overview of the framework and the channel content, it is not sufficient to explain the ^{29}Si MAS NMR spectrum. Indeed, there is only one crystallographic silicon site (Si1) in the average description of the new phase but two resonances of almost the same intensity on the ^{29}Si MAS NMR spectrum separated by 0.5 ppm (Figure S5). It could be explained by disorder involving distortions of the Si1 tetrahedra that are all of type Si-$(OSi)_3$(OZn). However, this assumption is not supported by single crystal 3D ED analysis, because the SiO_4 layer in the refined superstructure model does not appear significantly influenced by the superstructure (Figure 9a). A more likely explanation is the zinc/lithium ordering in the S2 and S3 tetrahedral sites (Figure 9b). The S2 and S3 cationic sites of the average model are split in three and four crystallographic sites respectively presenting different occupancies in the superstructure. The repartition of Zn and Li in those sites creates two different (Zn, Li)O_4 layers, with same average composition, that can explain the two different Si environments (Figure 10) seen on the ^{29}Si MAS NMR spectrum (Figure S5). These results are supported by the dynamical refinement of the supercell that leads to reasonable *R(obs)*/*wR(obs)* values of 0.1088/0.1120.

In the superstructure, O2 atoms (from O2-1 to O2-4) are not refined independently and create a unique tetrahedral environment. Thus, despite that Zn1-1, Zn1-2 and Zn1-3 have very different occupancies, they all possess the same oxygen environment. The situation is almost identical for Li atoms that are distributed in two distinct tetrahedral sites formed by O2, O4-1 and O4-2 (layers 1), and O2, O4-3 and O4-4 (layer 2). The layer of the superstructure labelled 2 is almost identical to the layer of the average one while the layer 1 presents a totally different cation ordering (Figure 9c). Interestingly, the average structure does not appear disordered on the ED data (Figure 6b): only the superstructure reflections $h = 2n+1$ are affected and elongated following the stacking direction *b*. The disorder observed might be due to different local cation orderings in some layers influencing the oxygen environment. This hypothesis is supported by the existence of at least one other ordering observed by 3D ED (see insert in Figure 4) and the presence of several small peaks in the powder data that remain unindexed.

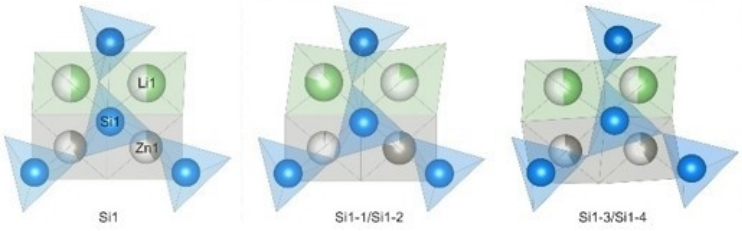

Figure 10. From the left to the right: unique Si environment present in the drying, were subsequently investigated as described below. average structure and the two Si environments due to a different repartition of Zn/Li in the (Zn, Li)O_4 layers of the main superstructure variant.

Because of its specific structure, the new microporous 10-MR zincolithosilicate has potential applications as radical scavenger in medicine for patients who need e. g., cardiopulmonary bypass or hemodialysis treatments. Indeed, it has been shown that VPI-7 (**VSV**), a 9-MR zincosilicate is effective to limit the reactive oxygen species (ROS) production and their damages at the level of human cells.[3b] A larger pore opening will facilitate the elimination by adsorption and ionic exchange of substrate such as Fe^{2+}/H_2O_2 species so limiting the Fenton reaction at the origin of ROS production. Before considering such an application, efforts in synthesis will be necessary in order to produce sufficient quantities for trials on a pilot scale.

Conclusion

In this work, the synthesis at high-pressure and the structure elucidation of a new lithium-rich zeolitic zincolithosilicate (to be named MZS-1: Marseille-zincosilicate-1) are reported. From 3D ED data, its average structure was solved and refined (using the dynamical theory). The characteristic zeolitic framework is described using an average unit cell in space group *Ccc*2. MZS-1 is a zeolitic 10-membered ring zincosilicate of chemical formula per unit cell $(SiO_2)_2Zn_{0.408}LiO(OH)_2(Li,H)_{2.184}$. Its structure is composed of undulated silicate layers made of fused 6-membered rings. The SiO layers are connected via vertices of disordered (Zn,Li)O_4 tetrahedra. The flexibility of ZnO_4 tetrahedra allows the substitution of Zn by an unusually high amount of Li as part of the framework. A weak superstructure doubles the average unit

cell parameter a_0. The structure solution and refinement from 3D PED data revealed that the repartition of the Zn and Li atoms T sites creates two different $(Zn,Li)O_4$ layers that explain the two different Si environments seen on the ^{29}Si MAS and ^{1}H decoupled ^{29}Si MAS NMR spectra. This structural investigation also shed new light on the reasons for the potential excellent catalytic behavior of zincosilicate zeolites with respect ROS elimination in biochemical applications, Na-zincosilicate **VSV** was successfully applied by us in this context.

Experimental Section

Synthesis. The high pressure hydrothermal method of synthesis is based on the hydrothermal conversion of glasses by dissolution, establishing a true (non-colloidal) solution and subsequent recrystallization from the supersaturated solution.[7a] Glass of composition: 1 Li_2O: 1 ZnO: 2.75 SiO_2 was molten at 1450 °C using Li-carbonate and the oxide precursors. The glass was placed in copper containers with distilled water added (75% of volume) and closed. No organic template substances were added. The container was placed in a high-pressure autoclave, sealed and heated to 80 °C or 145 °C, respectively. Once the temperatures were reached, the hydraulic pressure was adjusted to 300 MPa. The experiment was stopped after 28 days and repeated twice in order to assure reproducibility. The resulting synthesis products, after filtration, washing and drying, were subsequently investigated as described below.

Characterization. The laboratory powder X-ray diffraction (PXRD) data was collected between 5 and 50° 2θ (step 0.01°) in Debye-Scherrer geometry on a STOE STADI-P diffractometer equipped with a linear position-sensitive detector (6° in 2θ) and employing Ge-monochromated $CuK\alpha_1$ radiation (λ = 1.5406 Å). Elemental EDX analysis of representative nanocrystals was performed on a JEOL ARM-200F microscope, operating at 200 kV equipped with a JEOL Centurio wide area Silicon Drift Detector (SDD). Prior to the measurement, the sample was crushed and deposited on a carbon coated Au grid after sonication of the powder in chloroform. ^{29}Si (I = 1/2) Magic Angle Spinning (MAS) with ^{1}H decoupling solid state NMR spectrum was recorded with a Bruker Avance DSX-400 spectrometer at 79.54 MHz on a 4 mm CPMAS probe head, with a spinning frequency of 7 kHz. The π/2 pulse length was 4.5 µs, the recycle delay of 600 s and the number of scans 512. For the ^{1}H-^{29}Si Cross Polarization Magic Angle Spinning (CPMAS) spectrum, the spinning frequency was also 7 kHz, the π/2 pulse length was 4.5 µs, the contact time of 4 ms, the recycle delay 2 s with a number of scans of 2000. The ^{7}Li MAS spectrum was recorded using a spinning frequency of 10 kHz, with a π/2 pulse length of 2.5 µs. A number of 128 scans were collected with a recycle delay of 5 s. Tetramethylsilane and 1.0 M LiCl aqueous solution were used as chemical shift references. The decomposition of the ^{7}Li MAS NMR spectrum was performed with the dmfit software.[34] Thermogravimetric (TGA) analysis of the studied compound was performed under air on a TA Instruments TGA Q500 thermoanalyser with a heating rate of 5°C min^{-1} up to 600 °C. Thermo-X-ray diffraction data of the sample synthesized at 80°C were collected on a Siemens D5000 diffractometer at room temperature, the sample was previously heated under air in a furnace at 213, 250, 330 and 700°C, respectively.

For transmission electron microscopy (TEM) investigations, the white powder was deposited on an amorphous carbon coated copper grid. Precession assisted-3D electron diffraction (3D ED) data were collected[15,16] on a Philips CM120 electron transmission microscope (TEM) (U_{acc} = 120 kV, LaB_6) with the precession device Nanomegas Digistar and a side-mounted CCD camera Olympus Veleta with 14-bit dynamic range. 3D ED data sets of non-oriented patterns were recorded at 100 K on several crystals and the best one was used in the structural analysis (Figure S3). The precession angle was set to 1 degree. The tilt step of the goniometer between two consecutive frames was 1 degree too. A condenser aperture of 10 µm and low illumination setting were used to produce a semiparallel beam of 200–300 nm in diameter on the sample in order to reduce the electron dose. ED data were analysed using the computer programs PETS2.0[24] and JANA2006.[35] For each data set the result is a list of hkl indices with associated intensities and estimated standard deviations based on counting statistics. The refinements were performed using both kinematical and dynamical approaches ("kinematical refinement" and "dynamical refinement") implemented in JANA2006.[19]

For the Rietveld refinement, PXRD data were collected at room temperature on the beamline CRISTAL at the Synchrotron Soleil (France).[36] A monochromatic beam with a wavelength of 0.7294 Å was selected from the undulator beam using a double crystal Si(111) monochromator. Reference material LaB6 (SRM660a) was used as the standard for calibration of the wavelength. A 1 mm diameter glass capillary was filled with the white powder sample, which was mounted on a two circle diffractometer equipped with an analyzer consisting in a bank of 21 Si(111) crystals. With this setup, it took approximately half an hour in continuous scanning mode to collect the diffraction pattern. The final data set used for refinement was obtained from the precise superposition and addition of the data from the 21 channels. Jana2006 was used for the Rietveld refinement.

CSD 2055061 (for MZS-1) contains the supplementary crystallographic data for this paper. These data are provided free of charge by the joint Cambridge Crystallographic Data Centre and Fachinformationszentrum Karlsruhe Access Structures service

www.ccdc.cam.ac.uk/structures.

Acknowledgements

This work was supported by the Czech Science Foundation, project number 19-08032S using instruments of the ASTRA laboratory established within the Operation program Prague Competitiveness - project CZ.2.16/3.1.00/24510. We thank Nicolas Dairou for technical assistance in hydrothermal synthesis. The authors acknowledge CNRS, SOLEIL and the BAG ЯECIPROCS network for allowance of synchrotron radiation facilities (proposal 20171078). We thank Carole Isaac for the SEM micrographs and Loic Vidal for the EDX chemical analyses on TEM.

Conflict of Interest

The authors declare no conflict of interest.

[1] L. B. McCusker, C. Baerlocher, Stud. Surf. Sci. Catal. (Eds.: J. Čejka, H. van Bekkum), Elsevier, 2005, pp. 41–64.

[2] a) P. Andy, M. E. Davis, Ind. Eng. Chem. Res. 2004, 43, 2922–2928; b) M. A. Deimund, J. Labinger, M. E. Davis, ACS Catal. 2014, 4, 4189–4195; c) S. Kowalak, E. Janiszewska, M. Gierczynska, V. Dolata, N. Z. Evmiridis, T. Katranas, A. Vlessidis, V. Tsiatouras, F. Roessner, E. Schneider, Recent Advances in the Science and Technology of Zeolites and Related Materials, Parts A - C, Vol. 154 (Eds.: E. VanSteen, M. Claeys, L. H. Callanan), 2004, pp. 2200–2207; d) S. Kowalak, E. Szymkowiak, M. Gierczynska, G. Giordano, Impact of Zeolites and Other Porous Materials on the New Technologies at the Beginning of the New Millennium, Pts a and B, Vol. 142 (Eds.: R. Aiello, G. Giordano, F. Testa), 2002, pp. 351–358; e) M. Orazov, M. E. Davis, Chem. Sci. 2016, 7, 2264–2274.

[3] a) R. Li, S. Wang, D. Li, Y. Qin, J. Yu, Chem. J. Chinese U. 2017, 38, 1935–1940; b) J. Fromonot, P. Suchon, L. Bruzzese, N. Kipson, E. Fenouillet, B. Mallet, R. Guieu, O. Schäf, Microporous Mesoporous Mater. 2015, 201, 240–246.

[4] D. W. Breck, Zeolite Molecular Sieves, Structure, Chemistry and Use, John Wiley & Sons, New York, London, Sydney, Toronto, 1974.

[5] a) M. J. Annen, M. E. Davis, Microporous Mater. 1993, 1, 57–65; b) C. Rohrig, H. Gies, Angew. Chem. Int. Ed. 1995, 34, 63–65; Angew. Chem. 1995, 107, 125–127; c) Y. Sakamoto, H. Zhao, H. Gies, K. Yamamoto, U. Kolb, T. Ikeda, Dalton Trans. 2020, 49, 12960–12969.

[6] T. S. Ercit, J. Vanvelthuizen, Can. Mineral. 1994, 32, 855–863.

[7] a) H. Ghobarkar, O. Schäf, Y. Massiani, P. Knauth, in The Reconstruction of Natural Zeolites (Eds.: H. Ghobarkar, O. Schäf, Y. Massiani, P. Knauth), Springer US, Boston, MA, 2003, pp. 19–33; b) O. Schäf, Private communication.

[8] a) W. A. Dollase, C. R. Ross, Am. Mineral. 1993, 78, 627–632; b) M. A. Camblor, R. F. Lobo, H. Koller, M. E. Davis, Chem. Mater. 1994, 6, 2193–2199; c) S.-H. Park, H. Gies, B. H. Toby, J. B. Parise, Chem. Mater. 2002, 14, 3187–3196.

[9] a) M. J. Annen, M. E. Davis, J. B. Higgins, J. L. Schlenker, J. Chem. Soc. Chem. Commun. 1991, 1175–1176; b) C. Rohrig, H. Gies, B. Marler, Zeolites 1994, 14, 498–503.

[10] C. Baerlocher, L. B. McCusker, Database of Zeolite Structures. http://www.iza-structure.org/databases/.

[11] S. H. Park, P. Daniels, H. Gies, Microporous Mesoporous Mater. 2000, 37, 129–143.

[12] S.-H. Park, J. B. Parise, H. Gies, H. Liu, C. P. Grey, B. H. Toby, J. Am. Chem. Soc. 2000, 122, 11023–11024.

[13] K. Yamamoto, C. Ideta, T. Ikeda, Microporous Mesoporous Mater. 2020, 297, (110038)1–9.

[14] a) M. Gemmi, H. Klein, A. Rageau, P. Strobel, F. Le Cras, Acta Crystallogr. Sect. B 2010, 66, 60–68; b) U. Kolb, T. Gorelik, C. Kübel, M. T. Otten, D. Hubert, Ultramicroscopy 2007, 107, 507–513; c) U. Kolb, T. Gorelik, M. T. Otten, Ultramicroscopy 2008, 108, 763–772; d) W. Wan, J. Sun, J. Su, S. Hovmoller, X. Zou, J. Appl. Crystallogr. 2013, 46, 1863–1873.

[15] M. Gemmi, A. E. Lanza, Acta Crystallogr. Sect. B 2019, 75, 495–504.

[16] a) R. Vincent, P. A. Midgley, Ultramicroscopy 1994, 53, 271–282; b) E. Mugnaioli, T. Gorelik, U. Kolb, Ultramicroscopy 2009, 109, 758–765.

[17] Y. Lorgouilloux, M. Dodin, E. Mugnaioli, C. Marichal, N. Bats, P. Caullet, U. Kolb, J.-L. Paillaud, RSC Adv. 2014, 4, 19440–19449.

[18] a) M. O. Cichocka, Y. Lorgouilloux, S. Smeets, J. Su, W. Wan, P. Caullet, N. Bats, L. B. McCusker, J.-L. Paillaud, X. Zou, Cryst. Growth Des. 2018, 18, 2441–2451; b) X. Wang, Y. Shen, R. Liu, X. Liu, C. Lin, D. Shi, Y. Chen, F. Liao, J. Lin, J. Sun, Acta Crystallogr. Sect. B 2019, 75, 333–342.

[19] a) L. Palatinus, V. Petricek, C. A. Correa, Acta Crystallogr. Sect. A: Found. Crystallogr. 2015, 71, 235–244; b) L. Palatinus, C. A. Correa, G. Steciuk, D. Jacob, P. Roussel, P. Boullay, M. Klementova, M. Gemmi, J. Kopecek, M. C. Domeneghetti, F. Camara, V. Petricek, Acta Crystallogr. Sect. B 2015, 71, 740–751.

[20] M. Gemmi, E. Mugnaioli, T. E. Gorelik, U. Kolb, L. Palatinus, P. Boullay, S. Hovmöller, J. P. Abrahams, ACS Cent. Sci. 2019, 5, 1315–1329.

[21] S.-H. Park, H. Boysen, J. B. Parise, Acta Crystallogr. Sect. B 2006, 62, 42–51.

[22] H. d'Amour, W. Denner, H. Schulz, Acta Crystallogr. Sect. B 1979, 35, 550–555.

[23] S. Yu, D. K. Smith, S. B. Austerman, Am. Mineral. 1978, 63, 1241–1248.

[24] L. Palatinus, P. Brazda, M. Jelinek, J. Hrda, G. Steciuk, M. Klementova, Acta Crystallogr. Sect. B 2019, 75, 512–522.

[25] a) L. Palatinus, W. Steurer, G. Chapuis, J. Appl. Crystallogr. 2007, 40, 456–462; b) L. Palatinus, Acta Crystallogr. Sect. B 2013, 69, 1–16.

[26] G. Oszlanyi, A. Suto, Acta Crystallogr. Sect. A 2005, 61, 147–152.

[27] L. Palatinus, P. Brázda, P. Boullay, O. Perez, M. Klementová, S. Petit, V. Eigner, M. Zaarour, S. Mintova, Science 2017, 355, 166–169.

[28] M. T. B. Clabbers, T. Gruene, E. van Genderen, J. P. Abrahams, Acta Crystallogr. Sect. A 2019, 75, 82–93.

[29] T. Latychevskaia, J. P. Abrahams, Acta Crystallogr. Sect. B 2019, 75, 523–531.

[30] G. Steciuk, L. Palatinus, J. Rohlíček, S. Ouhenia, D. Chateigner, Sci. Rep. 2019, 9, 9156.

[31] M. A. Camblor, M. E. Davis, J. Phys. Chem. 1994, 98, 13151–13156.

[32] L. B. McCusker, R. W. GrosseKunstleve, C. Baerlocher, M. Yoshikawa, M. E. Davis, Microporous Mater. 1996, 6, 295–309.

[33] E. Lippmaa, M. Maegi, A. Samoson, G. Engelhardt, A. R. Grimmer, J. Am. Chem. Soc. 1980, 102, 4889–4893.

[34] D. Massiot, F. Fayon, M. Capron, I. King, S. Le Calvé, B. Alonso, J.-O. Durand, B. Bujoli, Z. Gan, G. Hoatson, Magn. Reson. Chem. 2002, 40, 70–76.

[35] V. Petříček, M. Dušek, L. Palatinus, JANA2006, the crystallographic computing system, Institute of Physics, Prague, 2006.

[36] a) A. Coati, L. M. G. Chavas, P. Fontaine, N. Foos, B. Guimarães, P. Gourhant, P. Legrand, J.-P. Itie, P. Fertey, W. Shepard, T. Isabet, S. Sirigu, P.-L. Solari, D. Thiaudière, A. Thompson, Eur. Phys. J. Plus 2017, 132, (174)1–9; b) J.-P. Itie, F. Baudelet, V. Briois, E. Elkaïm, A. Nadji, D. Thiaudière, X-Rays and Materials (Eds.: P. Goudeau, R. Guinebretière), 2013, pp. 1–47.